science.sciencemag.org/content/371/6526/296/suppl/DC1

Supplementary Materials for

Topological pumping of a 1D dipolar gas into strongly correlated prethermal states

Wil Kao*, Kuan-Yu Li*, Kuan-Yu Lin, Sarang Gopalakrishnan, Benjamin L. Lev†

*These authors contributed equally to this work.
†Corresponding author. Email: benlev@stanford.edu

Published 15 January 2021, *Science* **371**, 296 (2021)
DOI: 10.1126/science.abb4928

This PDF file includes:

Materials and Methods
Supplementary Text
Figs. S1 to S8
Table S1
References

Materials and Methods

BEC production

We follow the procedure in Ref. [48] to produce a ^{162}Dy BEC in the Zeeman sublevel $m_J = -8$ ($J = 8$), the absolute ground state. The atoms are loaded into a far-off-resonance single-beam optical dipole trap (ODT1) from a 741-nm magneto-optical trap (MOT). Instead of evaporating at 1.58 G, as in Ref. [48], we ramp the field to 26.69 G in less than 1 ms. The scattering length at this field value is 150(6) a_0, and we experimentally identified this field to be optimal for BEC production between the broad 22-G and 27-G Feshbach resonances; see Ref. [49] and Fig. S1. The ramp sequence avoids having to sweep through the dense Feshbach spectrum of Dy with a condensed gas, where heating due to inelastic three-body collisions becomes significant. This protocol yields a nearly pure BEC of $2.23(5) \times 10^4$ atoms after the atoms are transferred from ODT1 into a crossed dipole trap (ODT2) for forced evaporation. At the end of evaporation, the ODT2 trap frequency is set to $[\omega_x, \omega_y, \omega_z] = 2\pi \times [63.9(6), 11.8(3), 166.4(5)]$ Hz. The magnetic field axis is kept along the direction of gravity $\hat{z}$ in the above procedure. We then rotate the field to align the dipoles at the desired θ, where θ is the angle subtended by the dipole polarization and $\hat{x}$. The rotation is adiabatic such that no collective mode is excited. The amplitude of the bias field is kept constant so that it does not coincide with Feshbach resonance features during the rotation. This procedure minimizes three-body heating and atom loss. The density profile of the dipolar BEC can be determined by solving the Thomas-Fermi integral equation for each θ, as in Ref. [50].

Quasi-1D confinement

Quasi-1D dipolar gases have been created in 1D tubes of 2D optical latices in systems using Cr in the weakly repulsive interacting regime [51] and Dy in the regime of $\gamma \lesssim 10$ [21]. We realize such an array of quasi-1D tube-like traps in a 2D optical lattice by retroreflecting a pair of linearly polarized laser beams. The lasers are red-detuned by 6.2 GHz from the 741-nm Dy narrow-line transition [52]. The $\hat{y}$ and $\hat{z}$ lattice beams have waist radii of 150 μm and 195 μm, respectively. The Dy AC light shift is anisotropic with respect to the magnetic dipole polarization (constrained in the $\hat{x}$-$\hat{z}$ plane) as a result of its large tensor polarizability [53]. Therefore, as in previous work [21], we use a half-wave plate to set the polarization of the $\hat{y}$ lattice beam to always be orthogonal to the dipoles to maximize the lattice depth at each θ. By tuning the laser power, we set the lattice depth $V_0 = 30\, E_\mathrm{R}$, where $E_\mathrm{R}/\hbar = 2\pi \times 2.24$ kHz is the recoil energy of a lattice photon. This depth corresponds to a transverse trap frequency of $2\pi \times 25$ kHz and a harmonic oscillator length of $a_\perp = \sqrt{\hbar/m\omega_\perp} = 952\, a_0$, where a_0 is the Bohr radius. The typical axial frequency of the tubes is 40 Hz. The lattice depth is measured using the Kapitza-Dirac diffraction technique [54]. The tunneling rate between the tubes is estimated by using

$$\frac{J}{E_\mathrm{R}} \simeq \frac{4}{\sqrt{\pi}}\, s^{3/4} \exp\left(-2\, s^{1/2}\right), \tag{S1}$$

where $s = V_0/E_\mathrm{R}$ [55]. For our lattice, $s = 30$ and $J/\hbar = 2\pi \times 1$ Hz. Thus, tunneling is negligible during the 100 ms of total time needed to measure collective oscillations.

Magnetic field determination

To measure the bias field magnitude, we drive transitions between magnetic sublevels using a weak radiofrequency (RF) field along $\hat{z}$. As a result of dipole-induced spin relaxation [56], the atoms subsequently release their Zeeman energy as kinetic energy and are ejected from the trap. Resonance appears as an atom loss feature, with the RF frequency equal to the Zeeman energy spacing and, by extension, proportional to the bias field magnitude. As shown in Fig. S2A, the typical line shape is well approximated by a Gaussian. This procedure is performed after the atoms are loaded into the 2D lattice, yielding a field accuracy of ~2 mG for all fields and θ-values under consideration.

Molecular binding energy spectroscopy

The molecular binding energy E_B in both 3D and quasi-1D can be determined by inducing resonant molecular association [49, 57, 58, 59]. Similar to the bias field calibration measurements, we produce an oscillating magnetic field along $\hat{z}$ of the form $B(t) = B_\mathrm{avg} + B_\mathrm{mod}\sin(2\pi f_\mathrm{mod} t)$, where B_mod and f_mod are the amplitude and frequency of the modulation. The resonant condition ($f_\mathrm{mod} = f_0$) is $E_\mathrm{B} + hf_\mathrm{mod} - p_\mathrm{res}^2/m = 0$, where E_B is the molecular binding energy and p_res^2/m is the resonant continuum energy. Assuming the Wigner threshold law, the line shape of such a measurement is given by

$$W_l(f, f_0) \propto \int_0^\infty \exp\left(\frac{-\epsilon}{T'}\right) \epsilon^{l+1/2} L_\gamma(f, f_0 + \epsilon)\, d\epsilon, \tag{S2}$$

where ϵ is the collision energy, $L_\gamma(f, f_0 + \epsilon)$ is a Lorentzian of full width at half maximum of γ centered at $f_0 + \epsilon$, and T' is the temperature in units of frequency [57]. Assuming only s-wave collisions ($l = 0$) and very narrow intrinsic linewidth such that $L_\gamma(f, f_0 + \epsilon) \to \delta[\epsilon - (f - f_0)]$, we may use the simpler expression

$$W_0(f, f_0) \propto \exp[-(f - f_0)/T']\,(f - f_0)^{1/2} \tag{S3}$$

to fit the spectra to the blue side of the resonance. The typical asymmetric line shape is shown in Fig. S2B.

Characterization of contact interaction

Figure S1 shows our data revealing the three Feshbach resonances (FR 1, FR 2, and FR 3) of ^{162}Dy used in this experiment. A broader resonance (FR 4) at lower fields (21.93 G) also contributes to the scattering length determination. We conduct high-resolution atom loss spectroscopy across the experimentally relevant field range using an ultracold thermal gas in 3D. Atom loss features at the FR poles are also present under 1D confinement, as shown in Fig. S1. We note that FR 1 and FR 4 were first reported in Ref. [49]. In particular, the resonance poles of interest for the stiffness and energy measurements are located at $B_{01} \approx 26.90$ G and $B_{02} \approx 27.05$ G, and CIR 1 and CIR 2 are located just to the low-field side of these FRs, respectively. The coupling between these collisional channels can be neglected since the resonance widths are small, i.e., $\{\Delta_2, \Delta_3\} \sim 10$ mG $\ll \Delta_1 \approx 0.2$ G $\ll \Delta_4 \approx 3$ G. Thus, the magnetic field dependence of the 3D scattering length can be modeled as

$$a_\mathrm{3D}(B) = a_\mathrm{bg}\left(1 - \frac{\Delta_1}{B - B_{01}} - \frac{\Delta_2}{B - B_{02}} - \frac{\Delta_3}{B - B_{03}} - \frac{\Delta_4}{B - B_{04}}\right), \tag{S4}$$

where the background scattering length is denoted by a_{bg} [60].

Reference [49] reports two sets of Feshbach parameters based either on anisotropic expansion (AR) data or a combination of AR and E_{B} measurements in 3D, as summarized in Table S1. We repeat these measurements because, unfortunately, the fit covariance matrix required for error propagation of $a_{3\mathrm{D}}$ in Eq. (S4) is not provided in Ref. [49]. We conduct our measurements primarily around FR 1 to avoid the multitude of narrow resonance features overlapped with FR 4. These are too narrow to affect the results of this work, but they can complicate the scattering length measurements. Accurate determination of $a_{3\mathrm{D}}$ depends predominantly on the knowledge of the poles and widths of the three resonances FR 1–3 shown in Fig. S1. We note that of the two sets of fit parameters provided in Ref. [49], the AR-only measurements, valid for both $a_{3\mathrm{D}} > 0$ and $a_{3\mathrm{D}} < 0$, yield an a_{bg} that is within the uncertainty of our previously measured value taken around 5 G [61, 62]. We choose to use this value. To limit the number of free parameters, we fix the values of a_{bg}, B_{04}, and Δ_4 using this AR-only data. We then extract B_{0i} and Δ_i and their errors for $i = 1, 2, 3$ from our independent, high-resolution measurements of E_{B} in both 3D and quasi-1D. Similar to Ref. [49], we fit the 3D data in the field range $B > 26.85$ G using the corrected universal model

$$E_{\mathrm{B}}(B) = -\frac{\hbar^2}{m[a_{3\mathrm{D}}(B) - \bar{a}]^2}, \tag{S5}$$

where for Dy, the mean scattering length $\bar{a} = 0.956\, R_{\mathrm{vdW}}$ [63] and $R_{\mathrm{vdW}} = 80\, a_0$ [64]. For the 1D data, E_{B} of the confinement-induced dimers is implicitly given by

$$\frac{a_{3\mathrm{D}}}{a_\perp} = -\frac{\sqrt{2}}{\zeta(1/2, -E_{\mathrm{B}}/2\hbar\omega_\perp)}, \tag{S6}$$

where ζ is the Hurwitz zeta function [24]. This combined least-square fit yields the six Feshbach parameters and the associated symmetric covariance matrix. This matrix is given by

$$\boldsymbol{\Sigma} = \begin{array}{c|cccccc} & B_{01} & \Delta_1 & B_{02} & \Delta_2 & B_{03} & \Delta_3 \\ \hline \mathrm{B}_{01} & 2.2 & 7.2 & 0.1 & 1.2 & -0.1 & -0.4 \\ \Delta_1 & & 25.2 & 0.2 & 3.4 & -0.0 & -1.2 \\ \mathrm{B}_{02} & & & 0.3 & 1.0 & -0.0 & -0.0 \\ \Delta_2 & & & & 3.9 & 0.0 & -0.2 \\ \mathrm{B}_{03} & & & & & 0.3 & 0.6 \\ \Delta_3 & & & & & & 1.6 \end{array}, \tag{S7}$$

in units of mG^2. The fit result is shown in Table S1, and the E_{B} data are summarized in Fig. S3.

Excitation of breathing modes

The breathing mode of the trapped quasi-1D gas appears as modulations of the axial width; see Fig. S4 for example. The mode may be stimulated by an input perturbation, and there are two such perturbations we employ in this work depending on which is more effective at a particular $g_{1\mathrm{D}}$; a similar strategy was employed in Ref. [18]. The first method involves quenching the axial trap depth. To do so, we change the trap depth adiabatically with either an additional dipole trap beam or the lattice beams before quickly ramping the laser power back to the pre-quench value. This induces a breathing of the trapped gas. The second method relies on the fact that the mode can be weakly excited when we perform the B-field sweep to tune $a_{3\mathrm{D}}$ from that used for forced evaporation to its target value. This ramp is performed as fast as possible from the Thomas-Fermi (TF) gas regime, across the TG-regime, over the CIR, and into the sTG regime, in a similar fashion to Ref. [18]; a fast ramp is desirable due to the need to limit heating from the resonances traversed. In particular, we set the ramp duration to be $100\ \mu$s. Once at the target field, we wait 5 ms for the chamber eddy currents to settle before starting the oscillation measurements. The sweep is sufficiently adiabatic to stimulate no more than a weak excitation of the breathing oscillation and does not cause the system to jump the extensive energy gap between Lieb-Liniger eigenstates shown in Fig. 3. Moreover, the benignness of the ramp is manifest in the fact that we measure E/N's and R's consistent with that expected from ground states of the repulsive Lieb-Liniger (LL) model (i.e., before the first CIR); see the lowest-energy black circle points in Fig. 3 and Fig. S5. Sweeping across the discontinuity in g_{1D} is nonadiabatic, but continuous in the LL eigenspectrum and wavefunction [16, 19], which makes possible the smooth transitions from the TF to TG and TG to sTG regimes. The breathing of the gas is studied in time-of-flight using absorption imaging, and we ensure that the resulting breathing amplitude is within 10–20% of the equilibrium gas width after expansion; see also Ref. [18] for other examples of such measurements in 1D gas systems. In our system, the dipole mode frequency varies between 33 and 47 Hz, whereas the breathing mode frequency lies between 66 and 94 Hz.

Fitting of breathing oscillations

The expanded gas shape, after integration over the lattice directions, can be approximated by a Gaussian. The time evolution of the best-fit root-mean-square (rms) width can be modeled by a damped sinusoid

$$x_{\mathrm{rms}}(t) = a_0 \exp\left(-\frac{t}{\tau}\right) \sin(\omega_{\mathrm{B}} t + \phi) + a_1 t + a_2, \tag{S8}$$

where a_0 is the breathing amplitude, τ is the damping time of the oscillation, ω_{B} is the breathing frequency, ϕ is the breathing phase, a_1 encapsulates the increase in gas width due to heating processes, and a_2 denotes the equilibrium gas width. We use a standard least-square fitting routine to extract ω_{B}. Additionally, to further evaluate the quality of the frequency estimation, we employ a resampling fitting method that is similar to that in Ref. [65]. Specifically, we randomly sample 80% of the oscillation time series 1000 times. Each of the generated time series is then fit to Eq. (S8). We ensure that the resulting best-fit ω_{B} distribution is single-mode, and that the least-square fitting result lies within 1σ of the mean of the distribution.

Energy-per-particle measurements

The energy per particle E/N is manifest in the width of the momentum distribution. After holding the atoms in the lattice for varying time intervals, we rapidly tune a_{3D} to near zero before deloading the lattice using a 500-μs exponential ramp to release the gas for time-of-flight imaging. This protocol ensures that the expansion of the gas is ballistic. We note that the lattice deloading sequence constitutes a standard band-mapping operation along $\hat{y}$ and $\hat{z}$ [66], which leaves the momentum distribution along the tube axis $\hat{x}$ unaffected. We map out the time evolution of the axial momentum distribution of the gas when determining the mean width of the expanded gas for use in this E/N measurement. This is because state preparation may weakly excite the breathing mode. We can account for this time-dependent width by measuring the axial momentum distribution for a varying hold time in the lattice, not just at one hold time. Only 30 ms is needed to record this time evolution, and a constant-amplitude sinusoid with constant background is used to fit the evolution. This procedure reveals the kinetic part of the energy per particle of the system under investigation, denoted as E/N in the main text.

The theoretical value of the dimensionless energy per particle $e(\gamma)$ and kinetic energy per particle $e_k(\gamma)$ in the ground state can be found by numerically solving the Bethe ansatz equations; see Ref. [19] and citations therein. This formalism has been extended to sTG and higher excited states [13, 19]. We follow this approach to evaluate $e(\gamma)$ and $e_k(\gamma)$ for all of the parameter space we have experimentally explored, producing the curves in Fig. 3 of the main text and Fig. S6 below. The calculation is summarized here for a homogeneous system. The Bethe ansatz wavefunction consists of plane waves with a quasimomentum distribution $g(k)$ satisfying the following integral equations:

$$1 + 2\lambda \int_{-1}^{1} \frac{g(k')dk'}{\lambda^2 + (k'-k)^2} = 2\pi g(k), \tag{S9}$$

$$e(\gamma) = \frac{\gamma^3}{\lambda^3} \int_{-1}^{1} g(k) k^2 dk\,, \tag{S10}$$

$$\gamma \int_{-1}^{1} g(k)dk = \lambda. \tag{S11}$$

Numerically solving these equations yields eigenstates and $e(\gamma)$ within the first holonomy cycle [19, 67]. Equation (S9) is generalized using the methods described in Ref. [13] to allow $e(\gamma)$ to be solved for excited states in different holonomy cycles. Systematic shifts due to the underlying harmonic trap and varying atom number among tubes in our system must be accounted for before the measured E/N may be compared with theory. The first systematic is due to the single-tube harmonic trap. The kinetic energy of such a trapped system is

$$\mathcal{E}_{i,j} = \int \frac{\hbar^2 n_{i,j}^2(x)}{2m} e_k\big[\gamma_{i,j}(x)\big] n_{i,j}(x)dx, \tag{S12}$$

where $n_{i,j}(x)$ is the density profile for the tube index (i,j) estimated using the local density approximation along with knowledge of $e(\gamma)$ [38, 68] and $\gamma_{i,j}(x) = -2/a_{1\mathrm{D}} n_{i,j}(x)$. We then consider tubes with varying atom numbers and perform a weighted average based on the probability $P(M)$ of finding M atoms in a tube [28]. The total resulting calibration factor C can be referenced to the energy per particle in the central tube as follows

$$\frac{\mathcal{E}}{N} = \frac{\hbar^2 n_{0,0}^2}{2m} e_k\big(\gamma_{0,0}\big) \cdot C. \tag{S13}$$

To enable a direct comparison to the theory curve $e_k(\gamma)$, the measured data E/N in Fig. 3 of the main text are normalized by a factor $C \cdot \hbar^2 n_{0,0}^2/2m$ that is recalculated for each set of experimental parameters.

Notes on error analysis

We present some details concerning error analysis. The uncertainties in the dipole and breathing frequencies and E/N values are estimated from least square fit results. Specifically, these are the diagonal entries of the covariance matrix scaled by the reduced χ^2 [69]. The dominant source of error for the interaction related quantities is $a_{3\mathrm{D}}$, and the error is propagated using the covariance matrix Eq. (S7) in order to account for correlations between Feshbach parameters. We note that for those data near the zero crossing and point of divergence in $a_{3\mathrm{D}}$ (e.g., near the limits where $A^2 \to \infty$ and 0, respectively), standard error propagation based on a Taylor series yields a diverging uncertainty. For these cases, we instead use the max-min method that gives asymmetric confidence intervals. This method has similarly been used in Ref. [18]. Standard error propagation is employed elsewhere [69, 70].

Supplementary Text

Discussion of intertube DDI

The intertube spacing is 371 nm, half the lattice wavelength. Atoms in nearby tubes are able to interact via the long-range dipole-dipole interaction (DDI) [21]. However, these interactions are weak compared to the total kinetic and short-range interaction energies per atom (outside the weakly repulsive ground-state regime). Indeed, the collective oscillation data agree with the isolated single-tube predictions for the ground states of the nondipolar repulsive LL model, as demonstrated by the R data in Fig. S5. Thus, because the intertube DDI evidently plays little role in the repulsive LL model data *and* because the nondipolar 55° sTG data in Fig. 2A are not too dissimilar from that of the nondipolar Cs system [18], we conclude that the intertube DDI plays little role in the attractive LL model data of Figs. 2–4. That is, both the absolute and differential shifts of the data due to the intertube DDI seem to be small, and we believe that the dramatic, orders-of-magnitude effect on the sTG stability comes from the intratube DDI.

Stiffness data for ground states of the repulsive Lieb-Liniger model versus θ

For nondipolar gases, it is known that R transitions from 3 for a TF BEC (A^2 roughly between 1 and 100) before rising to 4 as $A^2 \rightarrow 0$ in the TG limit [37]. This expectation is borne out by our 55° data in Fig. S5A and those of the Cs experiment [18]. Moreover, this seems to be true regardless of θ, showing how little the DDI affects the ground state system.

Stiffness data for 90° excited states on the attractive branch of the second holonomy level

We show stiffness data for the attractive branch of the second holonomy level in Fig. S6. The Bethe ansatz prediction is also plotted [19]. Since thermal gases have the same stiffness, $R = 4$ (see inset of Fig. S8B) [37, 43], collective oscillation measurements cannot alone tell us whether these states are nonthermal. However, we can discern their nonthermal nature by sweeping in and out of this regime for various hold times before making measurements of E/N and R, as shown in Fig. 4 of the main text.

Absence of CIR shift

Several theoretical works predict a dependence of the CIR position on the DDI strength and/or angle [36, 71, 72, 73]. We do not observe any such shift in our molecular binding energy measurements, within experimental resolution. This might be due to the narrowness of the Feshbach resonances in Dy, or to their unusually complicated character [74], both not considered in those works.

Theory predictions of purely dipolar sTG gases

Theoretical results prior to the start of this work focused exclusively on purely dipolar models, in which the only interaction comes from the DDI [75, 76, 77, 78, 79, 80, 81]. As such, these cannot describe the case at hand wherein there is an interplay between the short-range contact interaction and the DDI and it is the cyclical manipulation of the contact that topologically pumps the system.

Contact-free, repulsive DDI sTG gases were predicted to exist in the ground state, if one takes the definition of the sTG to be a gas with correlations stronger than that of a TG gas, regardless of whether it is excited [75, 76, 77, 78, 79, 80]. Such correlations arise due to the long-range nature of the repulsive DDI, and not to quenching into any attractive potential. Such states are very different from the DDI-stabilized *excited*-state quenched sTG gases discussed here. Regardless, the repulsive DDI strength of Dy is insufficient to induce ground-state sTG gases at the densities explored. Reference [81] did consider quenching a purely dipolar gas into an excited state sTG gas by abruptly rotating the magnetic field angle from repulsive ($\theta = 90°$) to attractive ($\theta = 0°$). But again, they did not consider the simultaneous effect of a contact interaction or its use for topological pumping.

Stimulated by our work, the authors of Ref. [82] considered the repulsive *ground* state of a Lieb-Liniger model with the DDI perturbatively added. They report R versus A^2 curves very similar to those presented as solid lines in Fig. S5 that were calculated using a regularized 1D DDI.

Regularized 1D dipole-dipole interaction

References [75, 76, 77, 78, 81] employed the unregularized DDI in their 1D models. This contains the $1/r^3$ divergence when two atoms approach one another. However, in a quasi-1D trap, this divergence is smoothed out by the transverse degrees of freedom; the interaction must be regularized by integrating out these transverse degrees of freedom [21, 79, 80, 82]. This operation removes the divergence, replacing it with an extra delta function-like term while reducing the strength of the $1/r^3$ term at short distances.

We now address whether there might be any contribution of this effective short-range term to our experiment. Such a contribution would be manifest as a shift of the CIR versus θ. As we do not measure any such shift, nor any inconsistency with respect to nondipolar theory in the ground state, we conclude that the effect is negligible in our mapping of B to $a_{3\mathrm{D}}$. Thus, $g_{1\mathrm{D}}$ and γ are unaffected. Away from the CIR, the contact-like DDI contribution may be simply added to the van der Waals contribution, as in Ref. [21]. We follow this method to: 1) generate the solid R versus A^2 curves in Fig. S5, which are nearly indistinguishable from that derived by a perturbative calculation presented in Ref. [82]; and 2) determine the position of the vertical dotted line in Fig. 2C of the main text and in Fig. S7. An axial trap frequency of 40 Hz and $N = 35$ are used to determine the position.

Minimal state

In the main text, we considered cycles in which (in the ideal limit) each eigenstate is pumped to a higher-energy many-body eigenstate. We can also consider the reverse cycle: under this, some eigenstates map to "collapsed" states with large numbers of molecular clusters and a corresponding divergence of the energy in the unitary limit. These minimal states are defined as eigenstates of the Hamiltonian for which this inverse cycle leads to a divergence of eigenenergy [13]. In other words, this is a ground state that is tuned into a bound state via cycling $g_{1\mathrm{D}}$ backwards: tuning $g_{1\mathrm{D}} > 0$ to $g_{1\mathrm{D}} < 0$ directly (i.e., without crossing a CIR) induces a collapse just like in attractive BECs in higher dimensions. We demonstrate that in our system, the states with $g_{1\mathrm{D}} \to 0^+$ in the first holonomy level are minimal states by tuning them directly to $g_{1\mathrm{D}} \to 0^-$ by crossing $g_{1\mathrm{D}} = 0$. To do so, we produce a 1D BEC at a B-field of 29.805 G (beyond CIR 2) for the repulsive DDI configuration (90°) before performing the inverse cycle of $g_{1\mathrm{D}}$ from positive to negative through zero. This protocol ensures that the gas does not get pumped to higher holonomy levels via crossing a CIR and the resulting $g_{1D} \to \pm\infty$ divergence. As shown in Fig. S7B, the heating rate diverges shortly after the point where the van der Waals (attractive) and DDI (positive) contributions to $g_{1\mathrm{D}}$ cancel, indicating the onset of collapse due to bound-state formation. This is confirmed by the stiffness measurement in Fig. S7A, where we are unable to excite a well-defined breathing mode below the same A^2 at which the heating begins to significantly increase.

Heating measurements

We determine the heating rate of the system for all interaction strengths in the ground and excited states. These measurements are summarized in Fig. S8A. The experimental sequence is identical to the breathing mode measurements, and the kinetic energy per particle E/N for each hold time can be extracted from the squared RMS width of the expanded gas, whose profile along the tube direction is well approximated by a single Gaussian.

Heating seems to ensue only after a hold time of $t_0 \approx 100$ ms, which is longer than the final time of the collective oscillation measurements. The fitted width remains roughly constant before t_0. The E/N increases linearly after this, and the best-fit slope determines the heating rate. We do not observe enhanced heating when the gas is quenched into a breathing mode. Both observations suggest that thermal effects are of negligible influence on the breathing mode measurements.

While most measured heating rates are within 1σ of the mean value of 14 nK/s, some remarks on the outliers are in order. First, when $\theta = 0°$, the dipoles are in the prolate configuration (i.e., they are aligned with the symmetry axis of the cylindrical tubes). The DDI is attractive in such a trap where the trap aspect ratio $l = \omega_x/\omega_\perp < 1$, leading to an instability at the mean-field level of the dipolar BEC, even in the presence of a repulsive contact interaction. (See Ref. [83] for a discussion of fluctuation corrections.) In our system, $l = 0.002 \approx 0$, and the critical 3D scattering length $a_{3\mathrm{D,\,crit}}$ is approximately equal to the dipolar length $a_{\mathrm{dd}} = C_{\mathrm{dd}}\, m/12\pi\hbar^2 = 129\, a_0$, where $C_{\mathrm{dd}} = \mu_0\mu^2 = \mu_0(9.93\mu_{\mathrm{B}})^2$ is the DDI coupling constant for Dy, μ_0 is the vacuum permeability, and μ_{B} is Bohr magneton [42]. For the point labeled A in the TF regime, $a_{3\mathrm{D}} = 154(6)\, a_0$ and, the enhanced heating rate when the breathing oscillations are initiated may be attributed to this mean-field mechanical instability. The source of heating for points B and C might be due to many-body cluster formation, since they are near the collapse point.

Thermally driven crossover from a Thomas-Fermi to an ideal Bose gas

We study thermal effects on the equation-of-state of a TF gas in the ground state as an independent means of verifying the characteristic heating rate of the quasi-1D system. Specifically, we set $\theta = 90°$ and $A^2 \approx 7$ (before crossing CIR 1), where $R \approx 3$ suggests that the gas is deep within the TF regime. We hold the atoms in the lattice for a varying delay time before initiating the breathing oscillation measurement. As predicted by Yang-Yang thermodynamics [84], the transition from the TF ($R = 3$) to the ideal Bose gas ($R = 4$) regime occurs at a crossover temperature $T_{\rm co} = \sqrt{\gamma}\,\hbar^2 n_{\rm 1D}^2/2m$, where $\gamma = -2/n_{\rm 1D}a_{\rm 1D}$ is the dimensionless LL interaction parameter and $n_{\rm 1D}$ is the 1D linear density [85]. For our experimental parameters, $T_{\rm co} \approx 17$ nK. The data in Fig. S8B shows that it takes over 840 ms for R to rise to 4. Given the typical heating rate of 14 nK/s (see Fig. S8A), it would take ~ 1 s to cross over into the ideal Bose gas regime if we assume the initial gas temperature is much less than $T_{\rm co}$. This timescale is consistent with our data.

Comment regarding comparison of 55° and nondipolar Cs data in Ref. [18]

We first restate qualitative arguments regarding where along A^2 the collapse should occur for nondipolar gases [15]. The point roughly occurs when the sum length $Na_{\rm 1D}$ equals the width of the harmonic container, which is proportional to $\sqrt{N}a_{\parallel}$ for fermionized atoms; i.e., when $A = \sqrt{N}a_{\rm 1D}/a_{\parallel} = 1$. The collapse may be described in analogy to the classical gas of hard rods of length $a_{\rm 1D}$ [15]. The classical gas becomes infinitely stiff as the sum of the rod lengths $Na_{\rm 1D}$ equals the length of the container, whereas the stiffness of the quantum gas softens to zero in the collapse. The earlier collapse of our 0° data may be viewed in this picture as arising from the attractive DDI "elongating the rods."

Our nondipolar data for 55° (see Fig. 2A) is shifted by $\sim 10\times$ to the low-A^2 side with respect to the Cs data in Ref. [18], itself shifted somewhat to the low-A^2 side of the estimate given above (and the variational Monte Carlo data). The reason for these shifts is unknown. Theory is not yet able to predict where the data should intercept $R = 0$ for any trapped quantum system [16], let alone the dipolar gas, as this has to do with details of the complicated coupling to the multitude of cluster states. Variational Monte Carlo suggests the gas becomes unstable ($R \to 0$) at $A^2 = 0.6$, but this is only approximate [16]. The shift is likely nonuniversal in origin, as is the exact intercept of the data with $R = 4$ [16].

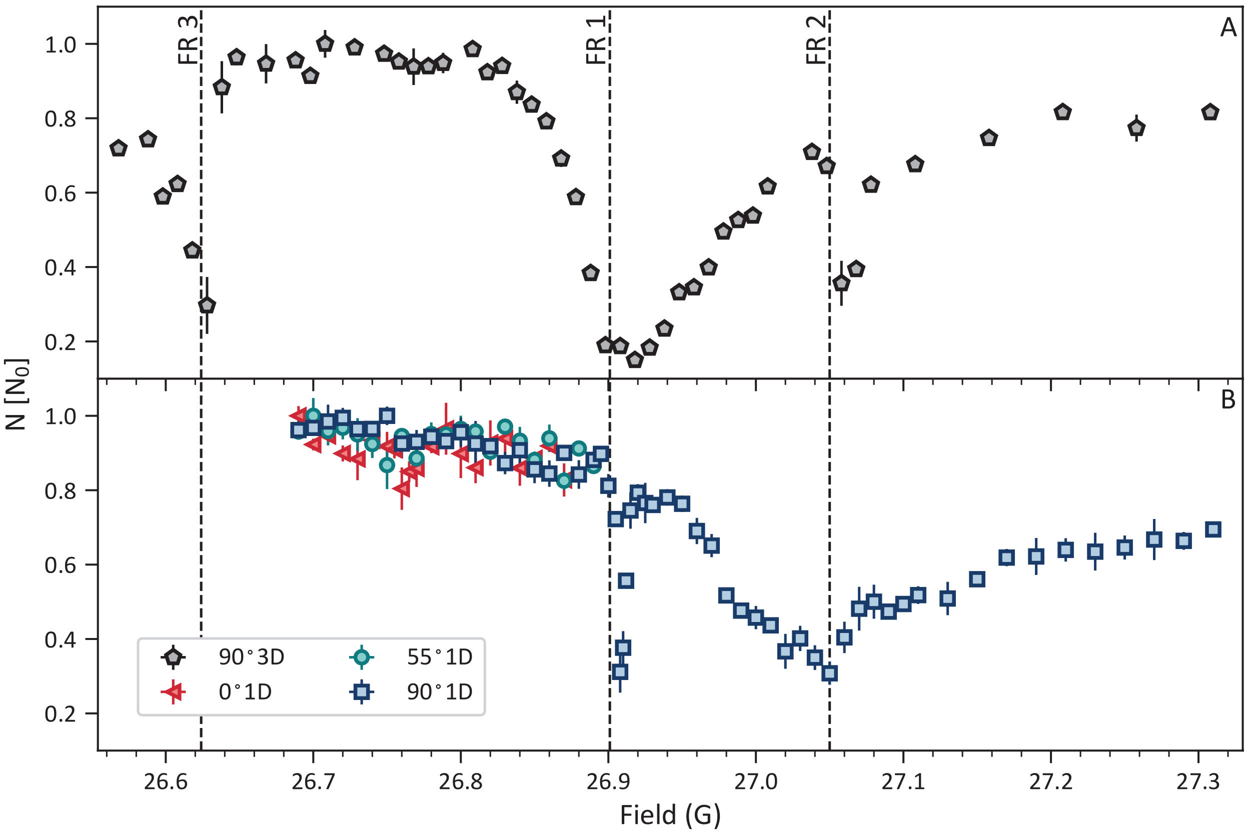

Fig. S1.

(A) Poles of the Feshbach resonances (FRs), indicated in dashed lines and determined from the molecular binding energy measurements, are overlaid on top of a high-resolution atom-loss spectrum taken using an ultracold thermal gas for a hold time of 50 ms in the lattice. (B) Atom-loss spectra in the 1D degenerate regime for the same lattice hold time are presented for the B-fields studied in Fig. 2 and Fig. S6 at each θ. In both panels, the atom number N is normalized by the peak number N_0 obtained in a field region away from any Feshbach resonance.

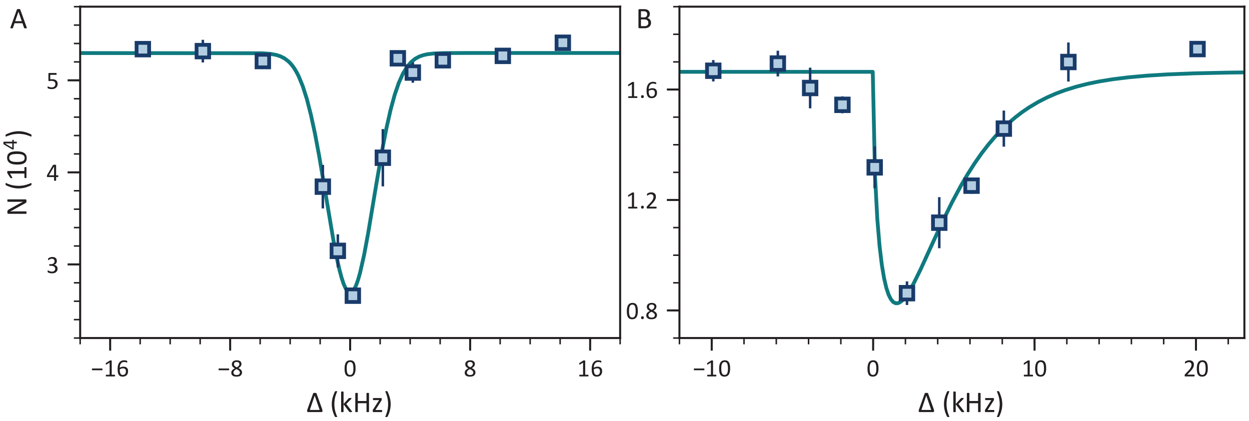

Fig. S2.

Typical atom loss spectra for (A) magnetic field and (B) molecular binding energy measurements. Here, N and Δ denote the atom number and RF detuning from the resonant condition, respectively. The solid lines are the best-fit line shape given by a Gaussian and W_0 [from Eq. (S3)] in the respective panels.

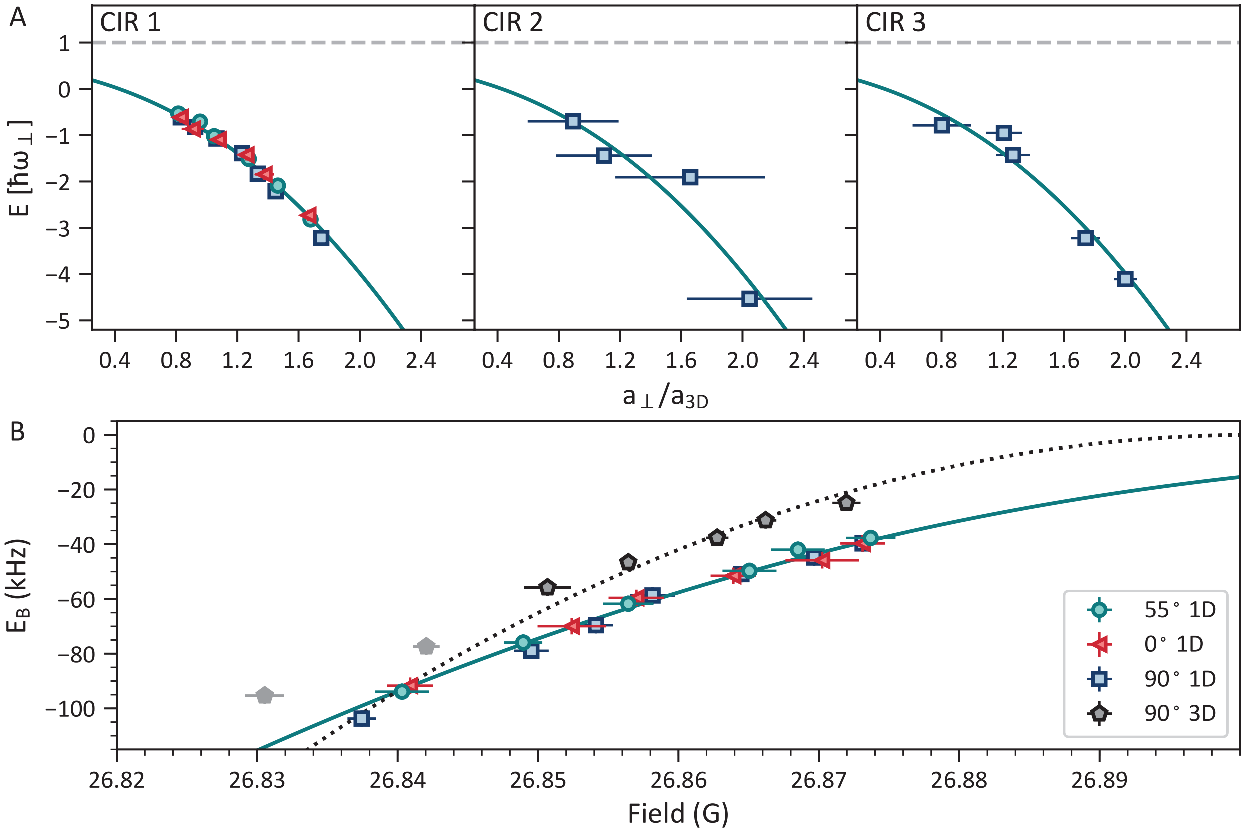

Fig. S3.

(A) Bound state energy data E under 1D confinement near the three CIRs as a function of the ratio of the transverse harmonic length ($a_\perp$) and 3D scattering length (a_{3D}). The open-channel energy is labeled in dashes. (B) 3D and 1D binding energy data E_{B} (defined as the energy difference between the open channel and the molecular bound state) around CIR 1 as a function of B-field. The best fit to the 3D model using Eq. (S5) and the 1D model using Eq. (S6) are shown in dotted and solid lines, respectively. We note that for the 3D data (pentagons), the points without dark edges are outside of the universal regime where $a_{\mathrm{3D}} \gg \bar{a}$ and are therefore excluded from the fit.

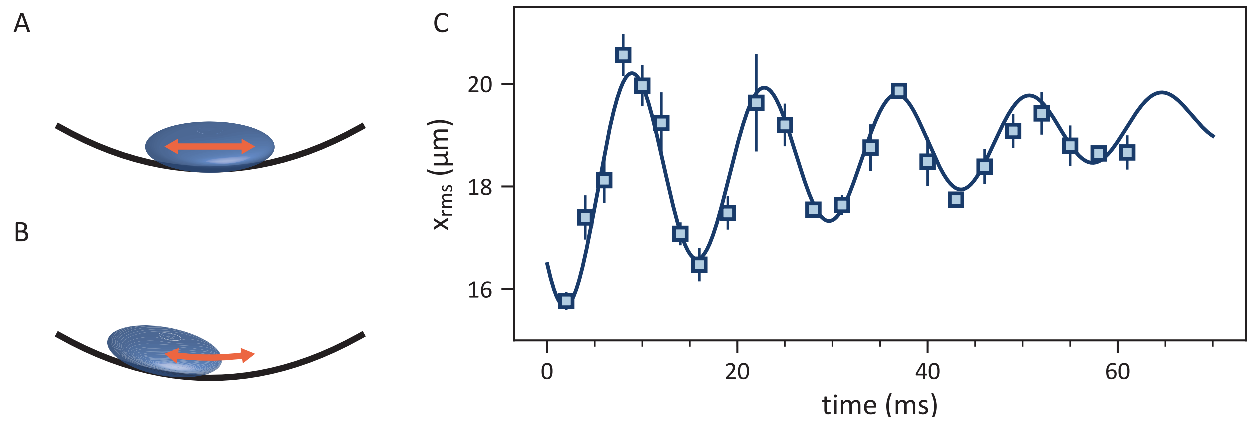

Fig. S4.
In stiffness measurements, we excite and compare the (A) breathing and (B) dipole modes of the gas confined within a weak harmonic trap along the axial direction $\hat{x}$. (C) Typical breathing data shows the time evolution of the rms cloud width x_{rms} after 14 ms of time-of-flight expansion. The fit to Eq. (S8) is shown as a solid line.

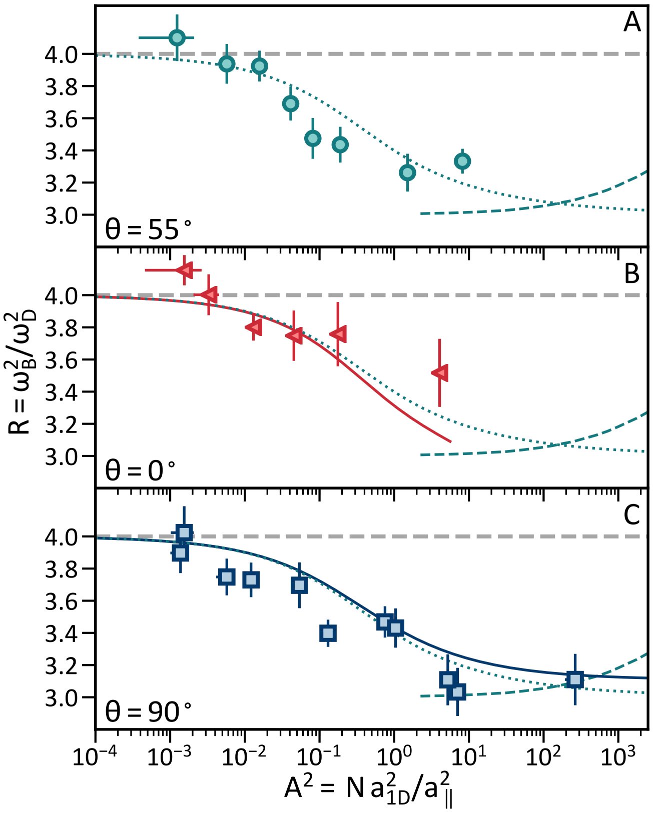

Fig. S5.

R versus interaction parameter A^2 in the repulsive $g_{1D} > 0$ regime of the first holonomy cycle. Measurements are shown for the (A) nondipolar ($\theta = 55°$), (B) attractive DDI (0°), and (C) repulsive DDI (90°) systems. Nondipolar theory (dotted line) describing the TF-to-TG crossover seems to agree with the data regardless of θ [37]. Accounting for corrections from the regularized 1D DDI provides a small shift from the nondipolar results, as shown in solid lines in panel (B) and (C). These lines are similar to that calculated in a recent perturbative treatment [82]. Regardless, these shifts are too small to be resolved by the experiment. We additionally show results of a nondipolar Hartree calculation (dashes) that describes the crossover of the TF gas into the weakly interacting regime of a Gaussian BEC [86].

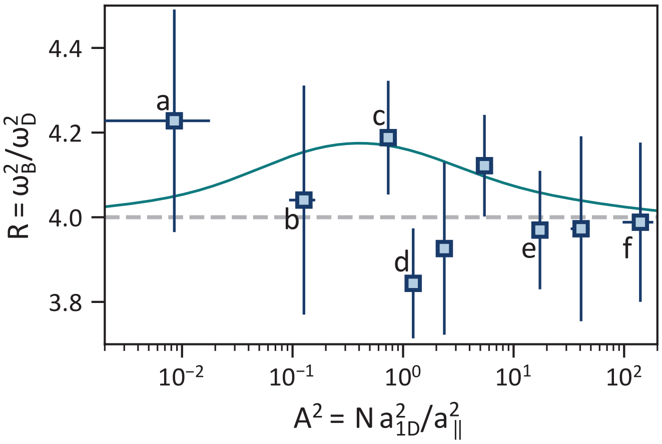

Fig. S6.

Stiffness R versus interaction parameter A^2 in the attractive $g_{1D} < 0$ regime of the second holonomy cycle for the repulsive DDI ($\theta = 90°$) system. Letter labels refer to the points in Figs. 1 and 3 of the main text. The solid curve is the Bethe ansatz prediction.

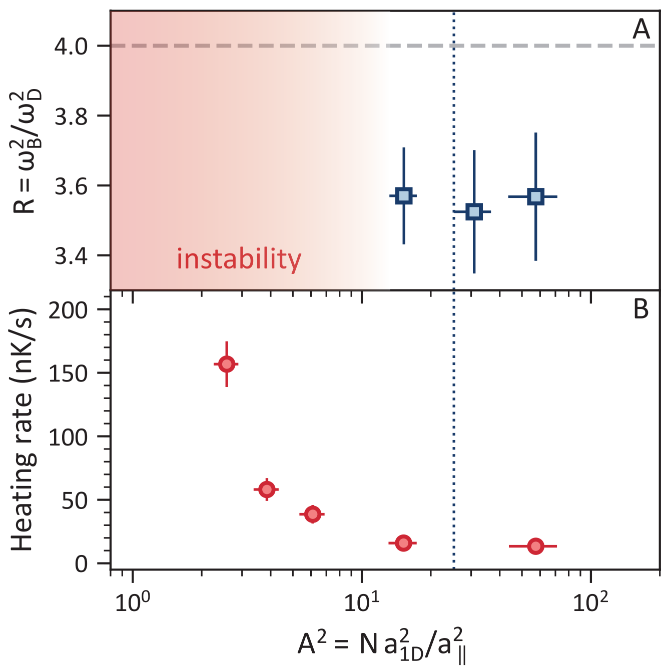

Fig. S7.

A minimal state [13] can be demonstrated by inverse cycling $g_{1\mathrm{D}}$ from positive to negative through zero (and not through the CIR-induced divergence), as described in the text. Stiffness and heating rate measurements for $g_{1\mathrm{D}} < 0$ are shown in panel (A) and (B), respectively. The vertical dotted line shows the point where the short-range DDI and van der Waals contributions to the 1D coupling strength are equal and opposite. The system becomes susceptible to collapse beyond this point (i.e., toward smaller A^2), where the attractive contact interactions begin to dominate the repulsive DDI. This collapse is manifest as a diverging heating rate and an R that softens to 0. In panel (A), breathing mode oscillations cannot be observed for A^2 less than ~ 10 due to this collapse instability.

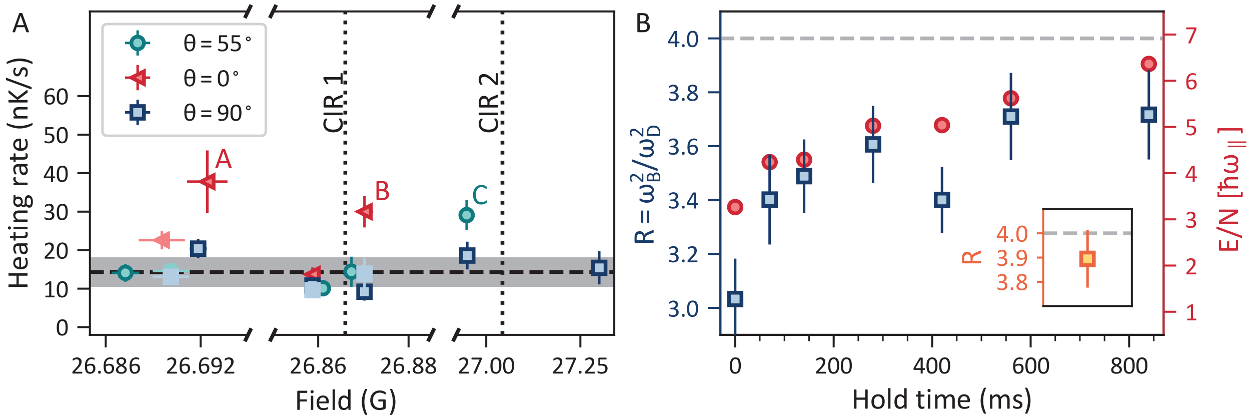

Fig. S8.

(A) Heating rate in 1D is plotted as a function of magnetic field, which provides tunability across different interaction regimes. The circles, triangles, and squares denote $\theta = 0°$, $55°$, and $90°$, respectively. The points with dark edges are measured after stimulating the breathing mode, whereas those without are at rest. The mean heating rate excluding the labeled outliners is shown in dashes, and the shaded area spans $\pm 1\sigma$ (standard deviation). Details regarding the three outlier points in the unstable regime for $\theta = 0°$ and $55°$ (labeled A, B, and C) are provided in the text. (B) Heating of a TF gas with $\theta = 90°$ and $A^2 = N\,a_{1\mathrm{D}}^2/a_{\parallel}^2 \approx 7$. The ratio $R = (\omega_{\mathrm{B}}/\omega_{\mathrm{D}})^2$ (squares) and kinetic energy per particle E/N (circles) are plotted as a function of the hold time before breathing oscillations are stimulated and measured. These data may be compared to the thermalization (without heating) of excited states in Fig. 4 of the main text. The inset shows the stiffness of a thermal gas at 160 nK.

Table S1.

Summary of Feshbach parameters for the four FRs included in Eq. (S4). We choose to report a covariance matrix for the errors in our measurements rather than an error on each entry in the table. The 6×6 covariance matrix $\mathbf{\Sigma}$ for B_{0i} and Δ_i for $i = 1, 2, 3$ is given in the text.

	a_{bg} (a_0)	B_{01} (G)	Δ_1 (G)	B_{02} (G)	Δ_2 (G)	B_{03} (G)	Δ_3 (G)	B_{04} (G)	Δ_4 (G)
Ref. [49]: AR	180(50)	26.892(7)	0.14(2)					21.93(20)	2.9(10)
Ref. [49]: AR+3D E_{B}	220(50)	26.902(4)	0.14(5)					21.91(5)	1.9(7)
This work	180	26.901	0.163	27.050	0.040	26.624	0.029	21.93	2.9

References and Notes

1. L. D’Alessio, Y. Kafri, A. Polkovnikov, M. Rigol, From quantum chaos and eigenstate thermalization to statistical mechanics and thermodynamics. *Adv. Phys.* **65**, 239–362 (2016). doi:10.1080/00018732.2016.1198134
2. M. Rigol, V. Dunjko, M. Olshanii, Thermalization and its mechanism for generic isolated quantum systems. *Nature* **452**, 854–858 (2008). doi:10.1038/nature06838 Medline
3. R. Vasseur, J. E. Moore, Nonequilibrium quantum dynamics and transport: From integrability to many-body localization. *J. Stat. Mech.* **2016**, 064010 (2016). doi:10.1088/1742-5468/2016/06/064010
4. D. A. Abanin, E. Altman, I. Bloch, M. Serbyn, *Colloquium* : Many-body localization, thermalization, and entanglement. *Rev. Mod. Phys.* **91**, 021001 (2019). doi:10.1103/RevModPhys.91.021001
5. H. Bernien, S. Schwartz, A. Keesling, H. Levine, A. Omran, H. Pichler, S. Choi, A. S. Zibrov, M. Endres, M. Greiner, V. Vuletić, M. D. Lukin, Probing many-body dynamics on a 51-atom quantum simulator. *Nature* **551**, 579–584 (2017). doi:10.1038/nature24622 Medline
6. N. Shiraishi, T. Mori, Systematic Construction of Counterexamples to the Eigenstate Thermalization Hypothesis. *Phys. Rev. Lett.* **119**, 030601 (2017). doi:10.1103/PhysRevLett.119.030601 Medline
7. C. J. Turner, A. A. Michailidis, D. A. Abanin, M. Serbyn, Z. Papić, Weak ergodicity breaking from quantum many-body scars. *Nat. Phys.* **14**, 745–749 (2018). doi:10.1038/s41567-018-0137-5
8. E. J. Heller, Bound-State Eigenfunctions of Classically Chaotic Hamiltonian Systems: Scars of Periodic Orbits. *Phys. Rev. Lett.* **53**, 1515–1518 (1984). doi:10.1103/PhysRevLett.53.1515
9. S. Moudgalya, S. Rachel, B. A. Bernevig, N. Regnault, Exact excited states of nonintegrable models. *Phys. Rev. B* **98**, 235155 (2018). doi:10.1103/PhysRevB.98.235155
10. F. Marcus Kollar, A. Wolf, M. Eckstein, *Phys. Rev. B* **84**, 054304 (2011). doi:10.1103/PhysRevB.84.054304
11. V. Khemani, C. R. Laumann, A. Chandran, Signatures of integrability in the dynamics of Rydberg-blockaded chains. *Phys. Rev. B* **99**, 161101 (2019). doi:10.1103/PhysRevB.99.161101
12. D. J. Thouless, Quantization of particle transport. *Phys. Rev. B* **27**, 6083–6087 (1983). doi:10.1103/PhysRevB.27.6083
13. N. Yonezawa, A. Tanaka, T. Cheon, Quantum holonomy in the Lieb-Liniger model. *Phys. Rev. A* **87**, 062113 (2013). doi:10.1103/PhysRevA.87.062113
14. S. Kasumie, M. Miyamoto, A. Tanaka, Adiabatic excitation of a confined particle in one dimension with a variable infinitely sharp wall. *Phys. Rev. A* **93**, 042105 (2016). doi:10.1103/PhysRevA.93.042105

15. G. E. Astrakharchik, D. Blume, S. Giorgini, B. E. Granger, Quasi-one-dimensional Bose gases with a large scattering length. *Phys. Rev. Lett.* **92**, 030402 (2004). doi:10.1103/PhysRevLett.92.030402 Medline

16. G. E. Astrakharchik, J. Boronat, J. Casulleras, S. Giorgini, Beyond the Tonks-Girardeau gas: Strongly correlated regime in quasi-one-dimensional Bose gases. *Phys. Rev. Lett.* **95**, 190407 (2005). doi:10.1103/PhysRevLett.95.190407 Medline

17. M. T. Batchelor, M. Bortz, X. W. Guan, N. Oelkers, Evidence for the super Tonks–Girardeau gas. *J. Stat. Mech. Theory Exp* **2005**, L10001 (2005). doi:10.1088/1742-5468/2005/10/L10001

18. E. Haller, M. Gustavsson, M. J. Mark, J. G. Danzl, R. Hart, G. Pupillo, H.-C. Nägerl, Realization of an excited, strongly correlated quantum gas phase. *Science* **325**, 1224–1227 (2009). doi:10.1126/science.1175850 Medline

19. S. Chen, L. Guan, X. Yin, Y. Hao, X.-W. Guan, Transition from a Tonks-Girardeau gas to a super-Tonks-Girardeau gas as an exact many-body dynamics problem. *Phys. Rev. A* **81**, 031609 (2010). doi:10.1103/PhysRevA.81.031609

20. P. Solano, Y. Duan, Y.-T. Chen, A. Rudelis, C. Chin, V. Vuletić, Strongly Correlated Quantum Gas Prepared by Direct Laser Cooling. *Phys. Rev. Lett.* **123**, 173401 (2019). doi:10.1103/PhysRevLett.123.173401 Medline

21. Y. Tang, W. Kao, K.-Y. Li, S. Seo, K. Mallayya, M. Rigol, S. Gopalakrishnan, B. L. Lev, Thermalization near Integrability in a Dipolar Quantum Newton’s Cradle. *Phys. Rev. X* **8**, 021030 (2018). doi:10.1103/PhysRevX.8.021030

22. See supplementary materials.

23. M. Olshanii, Atomic Scattering in the Presence of an External Confinement and a Gas of Impenetrable Bosons. *Phys. Rev. Lett.* **81**, 938–941 (1998). doi:10.1103/PhysRevLett.81.938

24. T. Bergeman, M. G. Moore, M. Olshanii, Atom-Atom Scattering under Cylindrical Harmonic Confinement: Numerical and Analytic Studies of the Confinement Induced Resonance. *Phys. Rev. Lett.* **91**, 163201 (2003). doi:10.1103/PhysRevLett.91.163201 Medline

25. H. Moritz, T. Stöferle, K. Günter, M. Köhl, T. Esslinger, Confinement induced molecules in a 1D Fermi gas. *Phys. Rev. Lett.* **94**, 210401 (2005). doi:10.1103/PhysRevLett.94.210401 Medline

26. E. Haller, M. J. Mark, R. Hart, J. G. Danzl, L. Reichsöllner, V. Melezhik, P. Schmelcher, H.-C. Nägerl, Confinement-induced resonances in low-dimensional quantum systems. *Phys. Rev. Lett.* **104**, 153203 (2010). doi:10.1103/PhysRevLett.104.153203 Medline

27. M. Girardeau, Relationship between Systems of Impenetrable Bosons and Fermions in One Dimension. *J. Math. Phys.* **1**, 516–523 (1960). doi:10.1063/1.1703687

28. B. Paredes, A. Widera, V. Murg, O. Mandel, S. Fölling, I. Cirac, G. V. Shlyapnikov, T. W. Hänsch, I. Bloch, Tonks-Girardeau gas of ultracold atoms in an optical lattice. *Nature* **429**, 277–281 (2004). doi:10.1038/nature02530 Medline

29. T. Kinoshita, T. Wenger, D. S. Weiss, Observation of a one-dimensional Tonks-Girardeau gas. *Science* **305**, 1125–1128 (2004). doi:10.1126/science.1100700 Medline

30. J. B. McGuire, Study of Exactly Soluble One-Dimensional N-Body Problems. *J. Math. Phys.* **5**, 622–636 (1964). doi:10.1063/1.1704156

31. M. Kormos, G. Mussardo, A. Trombettoni, Local correlations in the super-Tonks-Girardeau gas. *Phys. Rev. A* **83**, 013617 (2011). doi:10.1103/PhysRevA.83.013617

32. T. Giamarchi, *Quantum Physics in One Dimension*, International Series of Monographs on Physics (Clarendon, 2003).

33. M. A. Cazalilla, R. Citro, T. Giamarchi, E. Orignac, M. Rigol, One dimensional bosons: From condensed matter systems to ultracold gases. *Rev. Mod. Phys.* **83**, 1405–1466 (2011). doi:10.1103/RevModPhys.83.1405

34. C. Chin, R. Grimm, P. Julienne, E. Tiesinga, Feshbach resonances in ultracold gases. *Rev. Mod. Phys.* **82**, 1225–1286 (2010). doi:10.1103/RevModPhys.82.1225

35. G. De Rosi, G. E. Astrakharchik, S. Stringari, Thermodynamic behavior of a one-dimensional Bose gas at low temperature. *Phys. Rev. A* **96**, 013613 (2017). doi:10.1103/PhysRevA.96.013613

36. S. Sinha, L. Santos, Cold dipolar gases in quasi-one-dimensional geometries. *Phys. Rev. Lett.* **99**, 140406 (2007). doi:10.1103/PhysRevLett.99.140406 Medline

37. C. Menotti, S. Stringari, Collective oscillations of a one-dimensional trapped Bose-Einstein gas. *Phys. Rev. A* **66**, 043610 (2002). doi:10.1103/PhysRevA.66.043610

38. G. E. Astrakharchik, Local density approximation for a perturbative equation of state. *Phys. Rev. A* **72**, 063620 (2005). doi:10.1103/PhysRevA.72.063620

39. I. E. Mazets, J. Schmiedmayer, Thermalization in a quasi-one-dimensional ultracold bosonic gas. *New J. Phys.* **12**, 055023 (2010). doi:10.1088/1367-2630/12/5/055023

40. S. Tan, M. Pustilnik, L. I. Glazman, Relaxation of a high-energy quasiparticle in a one-dimensional bose gas. *Phys. Rev. Lett.* **105**, 090404 (2010). doi:10.1103/PhysRevLett.105.090404 Medline

41. I. E. Mazets, Integrability breakdown in longitudinaly trapped, one-dimensional bosonic gases. *Eur. Phys. J. D* **65**, 43–47 (2011). doi:10.1140/epjd/e2010-10637-5

42. T. Lahaye, C. Menotti, L. Santos, M. Lewenstein, T. Pfau, The physics of dipolar bosonic quantum gases. *Rep. Prog. Phys.* **72**, 126401 (2009). doi:10.1088/0034-4885/72/12/126401

43. H. Moritz, T. Stöferle, M. Köhl, T. Esslinger, Exciting collective oscillations in a trapped 1D gas. *Phys. Rev. Lett.* **91**, 250402 (2003). doi:10.1103/PhysRevLett.91.250402 Medline

44. B. Bertini, F. H. L. Essler, S. Groha, N. J. Robinson, Prethermalization and Thermalization in Models with Weak Integrability Breaking. *Phys. Rev. Lett.* **115**, 180601 (2015). doi:10.1103/PhysRevLett.115.180601 Medline

45. K. Mallayya, M. Rigol, W. De Roeck, Prethermalization and Thermalization in Isolated Quantum Systems. *Phys. Rev. X* **9**, 021027 (2019). doi:10.1103/PhysRevX.9.021027

46. A. J. Friedman, S. Gopalakrishnan, R. Vasseur, Diffusive hydrodynamics from integrability breaking. *Phys. Rev. B* **101**, 180302 (2020). doi:10.1103/PhysRevB.101.180302

47 W. Kao, K.-Y. Li, K.-Y. Lin, S. Gopalakrishnan, B. L. Lev, *Harvard Dataverse* (2020). https://doi.org/10.7910/DVN/H8LX1V.

48. Y. Tang, N. Q. Burdick, K. Baumann, B. L. Lev, Bose–Einstein condensation of ^{162} Dy and ^{160} Dy. *New J. Phys.* **17**, 045006 (2015). doi:10.1088/1367-2630/17/4/045006

49. E. Lucioni, L. Tanzi, A. Fregosi, J. Catani, S. Gozzini, M. Inguscio, A. Fioretti, C. Gabbanini, G. Modugno, Dysprosium dipolar Bose-Einstein condensate with broad Feshbach resonances. *Phys. Rev. A* **97**, 060701 (2018). doi:10.1103/PhysRevA.97.060701

50. I. Sapina, T. Dahm, N. Schopohl, Ground-state and collective modes of a spin-polarized dipolar Bose-Einstein condensate in a harmonic trap. *Phys. Rev. A* **82**, 053620 (2010). doi:10.1103/PhysRevA.82.053620

51. B. Pasquiou, G. Bismut, E. Maréchal, P. Pedri, L. Vernac, O. Gorceix, B. Laburthe-Tolra, Spin relaxation and band excitation of a dipolar Bose-Einstein condensate in 2D optical lattices. *Phys. Rev. Lett.* **106**, 015301 (2011). doi:10.1103/PhysRevLett.106.015301 Medline

52. M. Lu, S. H. Youn, B. L. Lev, Spectroscopy of a narrow-line laser-cooling transition in atomic dysprosium. *Phys. Rev. A* **83**, 012510 (2011). doi:10.1103/PhysRevA.83.012510

53. W. Kao, Y. Tang, N. Q. Burdick, B. L. Lev, Anisotropic dependence of tune-out wavelength near Dy 741-nm transition. *Opt. Express* **25**, 3411–3419 (2017). doi:10.1364/OE.25.003411 Medline

54. P. L. Gould, G. A. Ruff, D. E. Pritchard, Diffraction of atoms by light: The near-resonant Kapitza-Dirac effect. *Phys. Rev. Lett.* **56**, 827–830 (1986). doi:10.1103/PhysRevLett.56.827 Medline

55. I. Bloch, J. Dalibard, W. Zwerger, Many-body physics with ultracold gases. *Rev. Mod. Phys.* **80**, 885–964 (2008). doi:10.1103/RevModPhys.80.885

56. N. Q. Burdick, K. Baumann, Y. Tang, M. Lu, B. L. Lev, Fermionic suppression of dipolar relaxation. *Phys. Rev. Lett.* **114**, 023201 (2015). doi:10.1103/PhysRevLett.114.023201 Medline

57. K. M. Jones, P. D. Lett, E. Tiesinga, P. S. Julienne, Fitting line shapes in photoassociation spectroscopy of ultracold atoms: A useful approximation. *Phys. Rev. A* **61**, 012501 (1999). doi:10.1103/PhysRevA.61.012501

58. S. T. Thompson, E. Hodby, C. E. Wieman, Ultracold molecule production via a resonant oscillating magnetic field. *Phys. Rev. Lett.* **95**, 190404 (2005). doi:10.1103/PhysRevLett.95.190404 Medline

59. A. D. Lange, K. Pilch, A. Prantner, F. Ferlaino, B. Engeser, H.-C. Nägerl, R. Grimm, C. Chin, Determination of atomic scattering lengths from measurements of molecular binding energies near Feshbach resonances. *Phys. Rev. A* **79**, 013622 (2009). doi:10.1103/PhysRevA.79.013622

60. K. Jachymski, P. S. Julienne, Analytical model of overlapping Feshbach resonances. *Phys. Rev. A* **88**, 052701 (2013). doi:10.1103/PhysRevA.88.052701

61. Y. Tang, A. Sykes, N. Q. Burdick, J. L. Bohn, B. L. Lev, s -wave scattering lengths of the strongly dipolar bosons Dy 162 and Dy 164. *Phys. Rev. A* **92**, 022703 (2015). doi:10.1103/PhysRevA.92.022703

62. Y. Tang, A. G. Sykes, N. Q. Burdick, J. M. DiSciacca, D. S. Petrov, B. L. Lev, Anisotropic Expansion of a Thermal Dipolar Bose Gas. *Phys. Rev. Lett.* **117**, 155301 (2016). doi:10.1103/PhysRevLett.117.155301 Medline

63. G. F. Gribakin, V. V. Flambaum, Calculation of the scattering length in atomic collisions using the semiclassical approximation. *Phys. Rev. A* **48**, 546–553 (1993). doi:10.1103/PhysRevA.48.546 Medline

64. H. Li, J.-F. Wyart, O. Dulieu, S. Nascimbène, M. Lepers, Optical trapping of ultracold dysprosium atoms: Transition probabilities, dynamic dipole polarizabilities and van der Waals C_6 coefficients. *J. Phys. At. Mol. Opt. Phys.* **50**, 014005 (2016). doi:10.1088/1361-6455/50/1/014005

65. F. Görg, K. Sandholzer, J. Minguzzi, R. Desbuquois, M. Messer, T. Esslinger, Realization of density-dependent Peierls phases to engineer quantized gauge fields coupled to ultracold matter. *Nat. Phys.* **15**, 1161–1167 (2019). doi:10.1038/s41567-019-0615-4

66. M. Greiner, I. Bloch, O. Mandel, T. W. Hänsch, T. Esslinger, Exploring phase coherence in a 2D lattice of Bose-Einstein condensates. *Phys. Rev. Lett.* **87**, 160405 (2001). doi:10.1103/PhysRevLett.87.160405 Medline

67. E. H. Lieb, W. Liniger, Exact Analysis of an Interacting Bose Gas. I. The General Solution and the Ground State. *Phys. Rev.* **130**, 1605–1616 (1963). doi:10.1103/PhysRev.130.1605

68. V. Dunjko, V. Lorent, M. Olshanii, Bosons in cigar-shaped traps: Thomas-Fermi regime, Tonks-Girardeau regime, and in between. *Phys. Rev. Lett.* **86**, 5413–5416 (2001). doi:10.1103/PhysRevLett.86.5413 Medline

69. P. R. Bevington, D. K. Robinson, Data reduction and error analysis for the physical sciences; 3rd ed. (McGraw-Hill, New York, NY, 2003).

70. J. R. Taylor, An Introduction to Error Analysis: The Study of Uncertainties in Physical Measurements, 2nd ed. (University Science Books, 1996).

71. T. Shi, S. Yi, Observing dipolar confinement-induced resonances in quasi-one-dimensional atomic gases. *Phys. Rev. A* **90**, 042710 (2014). doi:10.1103/PhysRevA.90.042710

72. L. Guan, X. Cui, R. Qi, H. Zhai, Quasi-one-dimensional dipolar quantum gases. *Phys. Rev. A* **89**, 023604 (2014). doi:10.1103/PhysRevA.89.023604

73. P. Giannakeas, V. S. Melezhik, P. Schmelcher, Dipolar confinement-induced resonances of ultracold gases in waveguides. *Phys. Rev. Lett.* **111**, 183201 (2013). doi:10.1103/PhysRevLett.111.183201 Medline

74. A. Petrov, E. Tiesinga, S. Kotochigova, Anisotropy-induced Feshbach resonances in a quantum dipolar gas of highly magnetic atoms. *Phys. Rev. Lett.* **109**, 103002 (2012). doi:10.1103/PhysRevLett.109.103002 Medline

75. G. E. Astrakharchik, Y. E. Lozovik, Super-Tonks-Girardeau regime in trapped one-dimensional dipolar gases. *Phys. Rev. A* **77**, 013404 (2008). doi:10.1103/PhysRevA.77.013404

76. A. S. Arkhipov, G. E. Astrakharchik, A. V. Belikov, Y. E. Lozovik, Ground-state properties of a one-dimensional system of dipoles. *JETP Lett.* **82**, 39–43 (2005). doi:10.1134/1.2045336

77. R. Citro, E. Orignac, S. De Palo, M. L. Chiofalo, Evidence of Luttinger-liquid behavior in one-dimensional dipolar quantum gases. *Phys. Rev. A* **75**, 051602 (2007). doi:10.1103/PhysRevA.75.051602

78. P. Pedri, S. De Palo, E. Orignac, R. Citro, M. L. Chiofalo, Collective excitations of trapped one-dimensional dipolar quantum gases. *Phys. Rev. A* **77**, 015601 (2008). doi:10.1103/PhysRevA.77.015601

79. F. Deuretzbacher, J. C. Cremon, S. M. Reimann, Ground-state properties of few dipolar bosons in a quasi-one-dimensional harmonic trap. *Phys. Rev. A* **81**, 063616 (2010). doi:10.1103/PhysRevA.81.063616

80. F. Deuretzbacher, J. C. Cremon, S. M. Reimann, Erratum: Ground-state properties of few dipolar bosons in a quasi-one-dimensional harmonic trap [Phys. Rev. A **81**, 063616 (2010)]. *Phys. Rev. A* **87**, 039903 (2013). doi:10.1103/PhysRevA.87.039903

81. M. D. Girardeau, G. E. Astrakharchik, Super-Tonks-Girardeau state in an attractive one-dimensional dipolar gas. *Phys. Rev. Lett.* **109**, 235305 (2012). doi:10.1103/PhysRevLett.109.235305 Medline

82. S. De Palo, R. Citro, E. Orignac, Variational Bethe ansatz approach for dipolar one-dimensional bosons. *Phys. Rev. B* **101**, 045102 (2020). doi:10.1103/PhysRevB.101.045102

83. D. Edler, C. Mishra, F. Wächtler, R. Nath, S. Sinha, L. Santos, Quantum Fluctuations in Quasi-One-Dimensional Dipolar Bose-Einstein Condensates. *Phys. Rev. Lett.* **119**, 050403 (2017). doi:10.1103/PhysRevLett.119.050403 Medline

84. C. N. Yang, C. P. Yang, Thermodynamics of a One-Dimensional System of Bosons with Repulsive Delta-Function Interaction. *J. Math. Phys.* **10**, 1115–1122 (1969). doi:10.1063/1.1664947

85. T. Jacqmin, J. Armijo, T. Berrada, K. V. Kheruntsyan, I. Bouchoule, Sub-Poissonian fluctuations in a 1D Bose gas: From the quantum quasicondensate to the strongly interacting regime. *Phys. Rev. Lett.* **106**, 230405 (2011). doi:10.1103/PhysRevLett.106.230405 Medline

86. A. I. Gudyma, G. E. Astrakharchik, M. B. Zvonarev, Reentrant behavior of the breathing-mode-oscillation frequency in a one-dimensional Bose gas. *Phys. Rev. A* **92**, 021601 (2015). doi:10.1103/PhysRevA.92.021601